Published in IET Electric Power Applications
Received on 3rd May 2011
Revised on 2nd December 2011
doi: 10.1049/iet-epa.2011.0125

ISSN 1751-8660

Detection of stator core faults in large electrical machines

D.R. Bertenshaw[1] *A.C. Smith*[2] *C.W. Ho*[2] *T. Chan*[3] *M. Sasic*[4]

[1]*ENELEC Ltd, Lightwater GU18 5XX, UK*
[2]*Singapore Institute of Manufacturing Technology, Singapore 638075*
[3]*Aurecon Australia Pty Ltd, Victoria 3205, Australia*
[4]*Iris Power LP, Toronto, Canada L4V 1T2*
E-mail: drb@bertenshaw.org.uk

Abstract: Monitoring the health of large electrical machines, especially power station generators, is now an integral part of their operation to maintain and extend life. This work studies the use of electromagnetic sensors to detect inter-lamination insulation faults in the stator cores of large generators before they propagate to a level that can lead to catastrophic failure. The work develops a deeper understanding of the electromagnetic behaviour of core faults so that condition-monitoring sensors can be more specific about the location and severity of the fault. The study develops two new three-dimensional (3D) analytical models, one for predicting the fault current distribution in a stator core fault and the second for predicting the varying detection of such current by air-cored sensors. This further analysed the 3D detection efficiency of typical short fault lengths to compare with the two dimensional (2D) default of infinite-length faults. Different fault positions were modelled so that a clearer understanding of the location and severity of the fault is possible. These were validated on a specially constructed experimental test core that can impose controlled fault currents. The study also demonstrates how small core faults can escalate then self-limit radially, but may propagate axially into longer more damaging faults.

1 Introduction

The stator cores of large ac electrical machines, especially power station generators, are constructed from stacks of electrical steel laminations, each coated with a thin layer of electrical insulation to limit the influence of induced eddy currents in the core. Large generators (e.g. 500 MW) will weigh over 200 tonnes and contain some 200 000 such laminations. Maintaining the integrity of their insulation is important. If a number of laminations become electrically shorted together, they can allow significant eddy fault currents to flow, causing dangerous local 'hot-spots' which, even if modest, can affect the integrity and life expectancy of nearby conductor insulation [1].

Damage to the inter-laminar insulation can occur from a number of sources, such as inadequate or damaged lamination coating, fretting in a loose core, excessive burrs in processing, mechanical damage from foreign objects or burning of laminations in the region of a winding failure [2]. Left unattended, these can propagate and lead, in extreme cases, to the catastrophic failure of the generator [3]. The ability to detect incipient damage to the stator lamination insulation is therefore regarded as an important function of normal service testing.

There are several methods of determining generator inter-lamination insulation damage, with the principle off-line ones surveyed by Tallam *et al.* [4]. There remains no direct, online means of detection, although research into potential methods is reported [5]. The traditional method [6] requires a high-induced loop flux at 80–100% of the operating flux level, with infra-red thermography used to detect those areas where some insulation breakdown has occurred and is causing local heating. This test has the advantage that it directly detects the heating phenomena of concern; however, it has substantial drawbacks. The required power levels can be very high (>1 MVA) with consequent hazards to operators and machine from a temporary winding, the test takes several days to conduct and sub-surface faults are poorly detected.

2 Electromagnetic stator core fault detection method

The desire for a simpler test that can be more rapidly and safely deployed grew in the 1970s, and a low flux, non-destructive, electromagnetic detection technique, generally known as EL CID (ELectromagnetic Core Imperfection Detector) [7], was developed in 1978. This technique has been used worldwide since the 1980s and is regarded as a reliable test procedure for large turbine and hydro-generators and motors [8]. The method involves exciting the core at a low flux level, typically 4% of operating flux, using a temporary excitation winding inserted into the generator bore. Such a low flux level allows the test to be conducted with normal power sources and no heating risk. The fault currents induced in any damaged areas are

measured by sensing the magnetic fields resulting from them with a Chattock potentiometer.

The Chattock magnetic potentiometer [9] consists of a flexible, uniform, air-cored coil sensor whose voltage output is proportional to the line integral of the ac magnetic field along its length, and thus measures the local magnetomotive force (m.m.f.) as a magnetic potential difference (m.p.d.) on the surface of the core between its two ends. The majority of the fault's magnetic potential occurs in the air above the surface of the core because of the high permeability of the core iron and its laminated structure, and can thus be detected by the Chattock potentiometer. It is applied across the core teeth straddling a slot as shown in Fig. 1, and scanned axially along the slots with the output monitored.

The Chattock sensor detects the vector sum of all the electromagnetic effects occurring within the underlying core. In the EL CID test the m.p.d. is resolved into components in phase (PHASE) and in quadrature (QUAD) with the excitation current by a phase-sensitive detector [10]. Since the voltage induced in any fault circuit is in proportion to the rate of change of flux, the resultant fault current can be detected as that m.p.d. in quadrature to the flux. Thus, the resistive (heat-producing) element of the fault current component of the Chattock signal is indicated by the QUAD m.p.d, with the PHASE signal representing the excitation m.m.f. [11]. Although the EL CID method is proven to detect the fault current in a region, the Chattock only senses the resultant m.p.d. in that region, and does not provide any information regarding the distribution of the current. Nor is it well researched with what amplitude the fault signals from different parts of the stator core will be measured. This work builds on studies presented in an earlier paper [12], developing a more rigorous three-dimensional (3D) analysis of the fault currents and their detection, using models based on a real 48-slot generator rated at 71 MVA, with a bore diameter of 0.86 m, outer diameter = 1.78 m and a slot depth of 0.155 m.

Naturally an electromagnetic detection system would be best analysed by the use of a suitable finite-element electromagnetic model. However, to obtain useful results this needs to successfully model in 3D both the flux fields and induced currents, and adequately reflect the unique lamination structure where axial conductivity is repeatedly interrupted by fine air-gaps. This is a very challenging problem to create successful formulations that remain computable. Recent finite-element (FE) research [13–15] has proposed dual-mesh arrangements still in development, not yet validated by experiment. In consequence, this study has chosen to investigate the insights that can be achieved by the development of analytic models of stator core faults.

3 2D analytical model of fault current

The current flowing in an inter-laminar fault is practically impossible to measure directly. The fault current, however, can be determined analytically in its simplest form by considering the problem in a 2D space. This assumes the fault to be infinitely long and to flow strictly in the axial direction only, returning predominantly through the nearest keybar to the fault. In the model shown in Fig. 2, w is the radial width of the stator core back (0.303 m), μ_r is the relative permeability of the core, typically 2000 at 0.056 T peak core flux density (T_{pk}), and r_{mean} is the mean core radius (0.737 m).

The electromagnetic test flux is produced by injecting an excitation current I_{ex} through the centre of the stator bore. The magnetic flux flows circumferentially around the core and induces an electromotive force (e.m.f.) in the fault which drives the fault current. The single-turn self-inductance of the core fault, per unit axial length, can then be determined as

$$L_c = \frac{\mu_0 \mu_r w}{2\pi r_{mean}} \tag{1}$$

The average peak flux density $\hat{B}_c$ in the core, ignoring the stator teeth, is determined by the EL CID test, and at 4% of service flux will typically be 0.056 T_{pk}. The peak induced fault e.m.f. per unit length, where r_f is the resistance of the fault circuit per unit length, is therefore:

$$\begin{aligned} \hat{e}_f &= j\omega \hat{B}_c w \\ &= \hat{i}_f (r_f + j\omega L_c) \end{aligned} \tag{2}$$

The fault current flows axially down the fault returning along

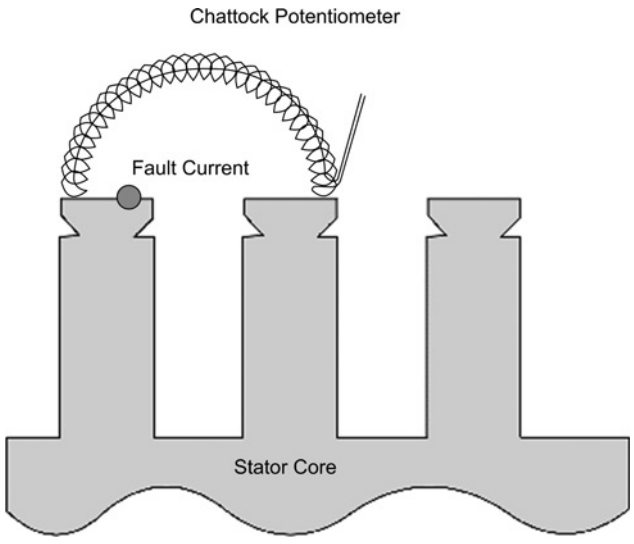

Fig. 1 *Chattock potentiometer positioned across a fault*

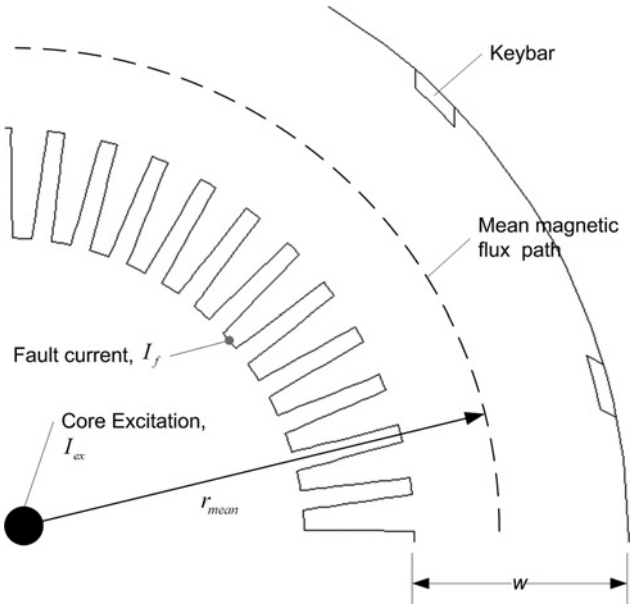

Fig. 2 *Stator core model*

doi: 10.1049/iet-epa.2011.0125

the keybar. In the 2D analysis the current path radially through the laminations is ignored; however, it is assumed to be a low impedance path for reasons discussed in Section 4. Similarly, the large cross-sectional area of the keybar ensures that its resistance is also very low in comparison, hence

$$r_{\mathrm{f}} = \frac{\rho_{\mathrm{f}}}{A_{\mathrm{f}}} \tag{3}$$

where ρ_{f} and A_{f} are the resistivity and cross-sectional area of the fault region. The peak fault current, $\hat{i}_{\mathrm{f}}$, is therefore

$$\hat{i}_{\mathrm{f}} = \frac{\mathrm{j}\omega \hat{B}_{\mathrm{c}} w}{r_{\mathrm{f}} + \mathrm{j}\omega L_{\mathrm{c}}} \tag{4}$$

The current in the fault circuit is thus largely determined by the fault region itself, because of the very low resistances of the lamination sheet material (several of which can also act in parallel) and keybar return. If the fault region grows in area as a result of further damage, the resistance decreases and the fault current increases. The fault circuit impedance ultimately changes (at approximately 1.8 mm fault radius) from predominantly resistive to inductive as the resistance falls, thus the fault current and power becomes limited by the core inductance as the fault expands.

Since the axial fault voltage is constant, the power developed in the fault will thus initially rise with the square of the fault radius, whereas the ability to dissipate the resultant heat by conduction will only rise in proportion to the radius (circumference) of the fault. Consequently, the equilibrium fault temperature will rise as the fault naturally progresses (usually mechanically). This can reach levels where thermal damage to the inter-laminar insulation is initiated, expanding the fault more rapidly to give a 'runaway' fault progression until the fault size is limited by the inductance [16]. Fig. 3 shows the power p.u. length developed in a fault at the lower relative permeability (970) typical of 1.5 T_{pk} service flux, which can potentially reach very high levels even in this modest-sized machine.

The model also demonstrates that even though a fault is self-limiting in radius, the power remains proportional to length. This permits the fault to continue to propagate axially without limit because of the temperature within the fault now being high enough to also progressively destroy the inter-lamination insulation at the fault's axial boundary. It gives rise to the well-known effect of melt-holes developing along the axis of the core in severe faults.

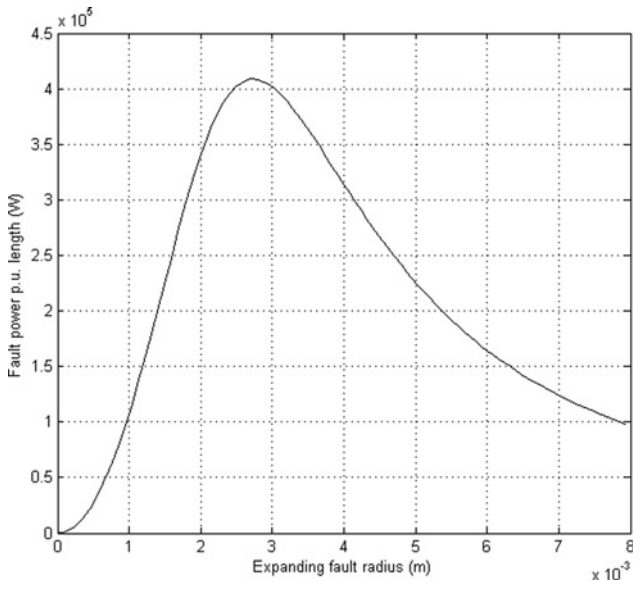

Fig. 3 *Fault power characteristics at 1.5 T_{pk}*

Table 1 Benchmark fault locations

Label	Fault location
1	tooth tip fault
2	tooth edge fault
3	slot base fault
4	core back fault between two adjacent slots
5	buried tooth fault
6	core back fault buried beneath a slot
7	core back fault near outer core periphery

A 2D Finite-Element model was also constructed and reported on by the authors [12], which compared the simulated sensor fault signals and the direct measurement of the quadrature fault current itself from the field solution. Faults were imposed as given in Table 1.

The results demonstrated clearly that the Chattock sensor provides an accurate measure of surface faults (faults 1–3) and a substantial proportion of faults located inside any particular tooth (fault 5). The predicted quadrature fault currents obtained from the 2D FE model above correlated closely with the fault current levels obtained from the 2D analytical model, and also from the 3D analytical model described in Section 5 of this paper for infinitely long faults.

4 3D analytical model of fault current distribution

Almost all embryonic faults are short, and, since they have return conduction paths down all the intermediate laminations, will not necessarily have the uniform current distribution assumed in the 2D model. The problem is essentially a 3D one, where the current path comprises the damaged region of the core, radially through the laminations and returning along the keybars at the back of the core. Thus, the analytical core fault model has to take into account the fault current path in the x, y and z directions.

The stator core is modelled as a homogenous cylindrical iron ring without the stator teeth, illustrated in Fig. 4 with the assumed fault current path ABCD. The shaft axis is directed in the z-direction and the magnetic flux flows circumferentially around the core in the x–y plane when the core is energised by the excitation coil. To simplify the analysis, it is assumed that only one single keybar nearest to the fault carries the lamination fault current.

The fault e.m.f. induced in an incremental element δz of the fault by the excitation current is

$$\delta \bar{E} = \mathrm{j}\omega \bar{B}_{\mathrm{c}} w \delta z \tag{5}$$

From Kirchoff's law applied to region AB, the current, $\bar{I}_z$ (z-directed fault current), shown in Fig. 4 is

$$\bar{I}_z = \frac{\delta z}{2}\left\{\bar{I}_{\mathrm{f}} + \left(\bar{I}_{\mathrm{f}} + \frac{\partial \bar{I}_{\mathrm{f}}}{\partial z}\delta z\right)\right\} + \bar{I}_z + \frac{\partial \bar{I}_z}{\partial z}\delta z \tag{6}$$

where $\bar{I}_{\mathrm{f}}$ is the lamination current density (A/m) and $\bar{I}_z$ is the axial fault current (A).

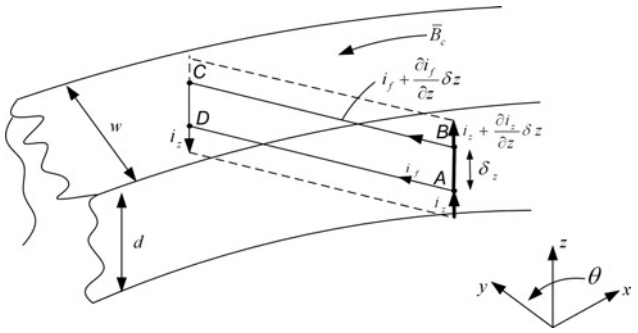

Fig. 4 *Fault current model*

Letting $\delta z \to 0$, this produces

$$\bar{I}_{\mathrm{f}} = -\frac{\partial \bar{I}_z}{\partial z} \tag{7}$$

With $\bar{Z}_{\mathrm{f}}$ and $\bar{Z}_z$ as the impedances of the laminations and z-directed fault paths, respectively, the induced voltage around loop $ABCD$, can be expressed as

$$\delta\bar{E} = \frac{1}{2}\left\{\bar{I}_z + \left(\bar{I}_z + \frac{\partial \bar{I}_z}{\partial z}\delta z\right)\right\}\bar{Z}_z\delta z + \left\{\left(\bar{I}_{\mathrm{f}} + \frac{\partial \bar{I}_{\mathrm{f}}}{\partial z}\delta z\right) - \bar{I}_{\mathrm{f}}\right\}\bar{Z}_{\mathrm{f}} \tag{8}$$

The radial resistance of the laminated core is not easily determined by analytical means. The current path therefore is assumed to have an effective return length, ℓ_{f}, and effective width, d, so that the resistivity of the radial path for a unit axial length is

$$r_{\mathrm{f}} = \frac{\rho_{\mathrm{f}}\ell_{\mathrm{f}}}{d}\ \Omega m \tag{9}$$

The inductance of the loop $ABCD$ can be divided into two components: that because of the current segments AB and CD; and that owing to the current distribution through AD and BC. The field produced by the current distribution, i_{f} through δz from AD to BC produces a complex field and eddy current distribution through the laminations and inter-laminar gaps. This inductance is assumed to be small in comparison with the inductance of the current segments AB and CD because of the low effective axial permeability caused by the inter-laminar gaps (core stacking factor). The total impedance through the laminations is thus

$$\bar{Z}_{\mathrm{f}} = r_{\mathrm{f}} \tag{10}$$

The inductance because of current segments AB and CD on the other hand is assumed to be dominated by the core inductance and can be approximated as

$$L_z = \frac{\mu_0\mu_{\mathrm{r}}w}{2\pi r_{\mathrm{mean}}} \tag{11}$$

The total impedance of the two z-directed fault current paths (fault and keybar) can therefore be expressed as

$$\bar{Z}_z = \left(\frac{\rho_{z1}}{A_{z1}} + \frac{\rho_{z2}}{A_{z2}}\right) + \mathrm{j}\omega L_z \tag{12}$$

Combining (5) and (8) we obtain

$$\mathrm{j}\omega\bar{B}_{\mathrm{c}}w = \bar{I}_z\bar{Z}_z + \frac{1}{2}\frac{\partial \bar{I}_z}{\partial z}\bar{Z}_z\delta z + \frac{\partial \bar{I}_{\mathrm{f}}}{\partial z}\bar{Z}_{\mathrm{f}} \tag{13}$$

and as $\delta z \to 0$, combining with (7) gives

$$\mathrm{j}\omega\bar{B}_{\mathrm{c}}w = \bar{I}_z\bar{Z}_z - \frac{\partial^2 \bar{I}_z}{\partial z^2}\bar{Z}_{\mathrm{f}} \tag{14}$$

The general solution to this differential equation is

$$\bar{I}_z(z) = A\cosh(\gamma z) - B\sinh(\gamma z) + \frac{\mathrm{j}\omega\bar{B}_{\mathrm{c}}w}{\bar{Z}_z} \tag{15}$$

where

$$\gamma^2 = \frac{\bar{Z}_z}{\bar{Z}_{\mathrm{f}}} \tag{16}$$

The boundary conditions $\bar{I}_z = 0$ at $z = 0$ and $z = d$ are used to determine the constants A and B. The axial fault current $\bar{I}_z$ is thus finally determined as

$$\bar{I}_z(z) = \frac{\mathrm{j}\omega\bar{B}_{\mathrm{c}}w}{\bar{Z}_z}\left\{1 - \cosh(\gamma z) - \left[\frac{1-\cosh(\gamma d)}{\sinh(\gamma d)}\right]\sinh(\gamma z)\right\} \tag{17}$$

This equation describes the fault current as a function of the axial position on the core surface. Fig. 5 shows the typical fault axial current distribution for different fault lengths, using the same core geometry and 0.45 mm diameter. Nickel–chromium (Ni–Cr) resistance wire (resistivity 1.08 μΩm) to simulate faults and allow a comparison with the experimental test core. The axial centre of the fault is at the $z = 0$ position, peak flux density of 0.056 T_{pk}, and radial current width (d) set at 10 mm.

Fig. 5 also shows that although the maximum axial fault current flowing through the damaged region in the core occurs at the centre of the fault in the axial direction as expected, it is essentially uniform along the fault except for short faults. As the fault grows, the maximum achievable axial fault current using (17) is

$$\bar{I}_z = \frac{\mathrm{j}\omega\bar{B}_{\mathrm{c}}w}{\bar{Z}_z} \tag{18}$$

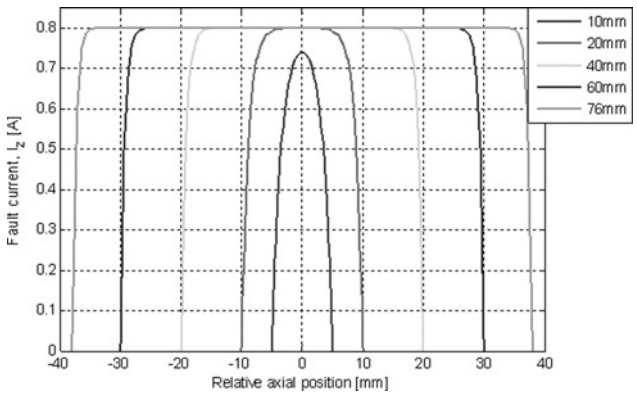

Fig. 5 *Axial peak fault current distribution for 10, 20, 40, 60 and 76 mm long faults*

doi: 10.1049/iet-epa.2011.0125

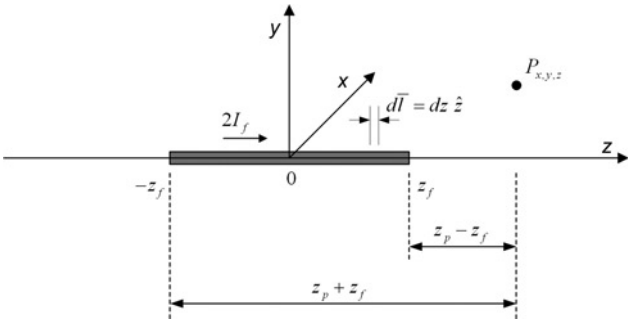

Fig. 6 *Derivation of the field distribution at any general point, P, in space*

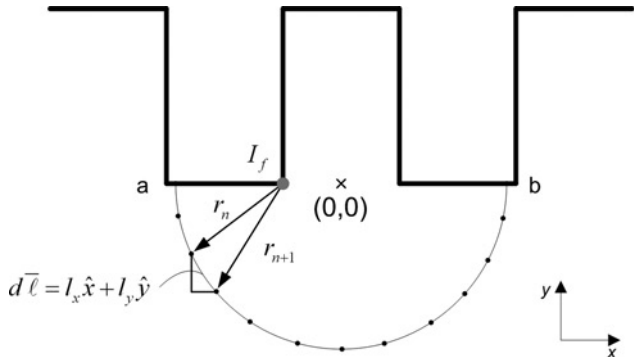

Fig. 7 *Evaluating the line integral path for an off-centred fault*

This is clearly independent of the fault length because both the induced e.m.f. and the resistive-dominated impedance scale linearly with fault length. The fault current will be limited by the inductive reactance only when the fault resistance has reduced because of a sufficient fault cross-sectional area as the fault grows thermally.

The maximum achievable axial fault current given above is the value predicted, as expected, by the 2D analytical model at 0.056 T_{pk} flux. The 2D analytical model therefore can be useful in obtaining an estimate of the peak fault current in long faults but the 3D analytical model is necessary to determine the variation in the fault current along the axial length of a finite-length fault. However, neither model allows a prediction of the signal detected by the Chattock sensor for a finite-length fault, which requires a more complex 3D analysis.

5 3D analytical model of Chattock signal detection

For surface core faults the Method of Images can be used to model the influence of the core, assuming that the core is homogeneous and infinitely permeable. Integrating the field along the Chattock path then produces a simulation of the Chattock fault signal on the bore. This technique enables a means of predicting the Chattock signal for finite-length, surface faults using a 3D analytical model. The Method of Images approach allows the field produced by a current-carrying filamentary fault element of finite length to be simulated by an infinitely permeable plane, with double the fault current $2I_{\text{f}}$. The Biot–Savart law can then be used to determine magnetic flux, $\overline{B}$ at any point in space around the finite-length fault current, by summing up the elemental field contributions along the fault length. Fig. 6 shows a fault with a length of $2Z_{\text{f}}$ on an infinitely permeable plane z–x, and an arbitrary point P in space at which the flux density is to be determined.

The coordinates of P at which the flux density is to be determined and the differential elemental point, P_{dl}, in the current-carrying element are as follows:

$$\begin{aligned} P &= x_p\hat{x} + y_p\hat{y} + z_p\hat{z} \\ P_{dl} &= 0\hat{x} + 0\hat{y} + z\hat{z} \end{aligned} \tag{19}$$

The distance, $\bar{r}$ between point P and P_{dl} is thus

$$\bar{r} = x_p\hat{x} + y_p\hat{y} + (z_p - z)\hat{z} \tag{20}$$

and also

$$r = \sqrt{x_p^2 + y_p^2 + (z_p - z)^2}, \quad \text{hence } \hat{r} = \frac{\bar{r}}{r} \tag{21}$$

Applying Biot–Savart, the flux density at the point P is expressed as follows

$$\bar{B}_p = \frac{\mu_0 2\bar{I}_{\text{f}}}{4\pi}\int_{-z_{\text{f}}}^{z_{\text{f}}} \frac{\hat{z}\times\hat{r}}{r^2}\,\text{d}z \tag{22}$$

Manipulating (22) with (20) and (21), and substituting $v = z_p - z$ and $\text{d}v = -\text{d}z$, yields

$$\bar{B}_p = \frac{\mu_0\bar{I}_f}{2\pi}\int_{z_p+z_{\text{f}}}^{z_p-z_{\text{f}}} \frac{y_p\hat{x} - x_p\hat{y}}{[(x_p^2 + y_p^2) + v^2]^{3/2}}\,\text{d}v \tag{23}$$

Solving the integral, the flux density at point $\bar{P}$ is given by equation (24)

The expression described in (24) can be used to determine the flux density for any arbitrary point in space away from the fault. This expression consists of only two space vector field components since the z-directed fault current can only produce fields in the x–y plane.

To obtain the Chattock signal for a fault position, the total flux linking the (typically) semi-circular Chattock path needs to be numerically evaluated. This approach assumes that the fault lies on the surface of an infinitely permeable plane which means that the slots shown in Fig. 7 are effectively filled with core steel. Although any arbitrary path could be chosen, the Chattock path was discretised into 37 evenly

$$\begin{aligned} \bar{B}_p = {} & \frac{\mu_0\bar{I}_{\text{f}}}{2\pi(x_p^2 + y_p^2)}\left\{\frac{(z_p - z_{\text{f}})y_p}{[x_p^2 + y_p^2 + (z_p - z_{\text{f}})^2]^{1/2}} - \frac{(z_p + z_{\text{f}})y_p}{[x_p^2 + y_p^2 + (z_p + z_{\text{f}})^2]^{1/2}}\right\}\hat{x} \\ & + \frac{\mu_0\bar{I}_{\text{f}}}{2\pi(x_p^2 + y_p^2)}\left\{\frac{(z_p + z_{\text{f}})x_p}{[x_p^2 + y_p^2 + (z_p + z_{\text{f}})^2]^{1/2}} - \frac{(z_p - z_{\text{f}})x_p}{[x_p^2 + y_p^2 + (z_p - z_{\text{f}})^2]^{1/2}}\right\}\hat{y} \end{aligned} \tag{24}$$

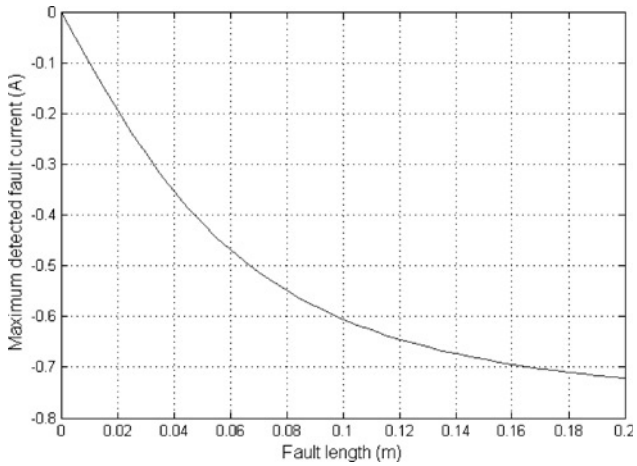

Fig. 8 *Apparent fault current at $z = 0$ mm plane for a -0.8 A peak fault located on the tooth edge*

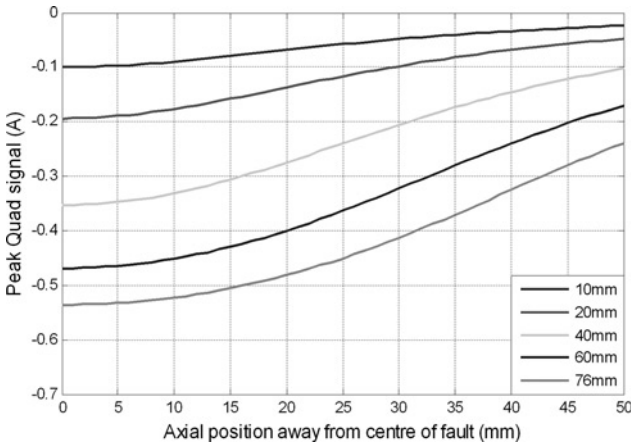

Fig. 9 *Analytical prediction of the Chattock axial scan fault signal for 10°, 20, 40, 60 and 76° mm long fault located on the tooth edge*

spaced segments as also shown in Fig. 7 to approximate the locus of a typical Chattock coil. The flux density at each discrete point was solved using (24), followed by a summation of all the elemental $\bar{H}d\bar{l}$ contributions

$$\int_a^b \bar{H}d\bar{l} \simeq \sum_a^b \bar{H}_n d\bar{l}_n \simeq \frac{1}{\mu_0}\sum_a^b (\bar{B}_{x\_n} l_{x\_n}\hat{x} + \bar{B}_{y\_n} l_{y\_n}\hat{y}) \qquad (25)$$

where $d\bar{\ell} = l_x\hat{x} + l_y\hat{y}$ is the distance between two adjacent coordinate points.

Equation (25) is used to evaluate the line integral path on the $z = 0$ mm plane where the strength of the field is at its maximum. The Chattock coil spans 84 mm across a slot and the fault with a fixed peak current of -0.8 A is located on the tooth edge as shown in Fig. 7. The apparent fault current detected by the Chattock coil for increasing fault length is shown in Fig. 8. This shows that the signal pickup of the Chattock sensor is greatly influenced by the length of the fault, with full current detection possible only if the fault length is long when the result converges to the 2D field value.

The analytical field distribution model was also applied to determine the signal from an axial scan along the surface of the core. The Chattock coil spanning 84 mm across a fault is initially positioned on the $z = 0$ mm plane where the centre of the fault lies, and then transverses along the z-direction away from fault. A series of simulations are performed for various fault lengths and for a current of -0.8 A peak (the current induced in a 0.45 mm diameter. Nichrome (NiCr) wire at 0.056 T_{pk}), with the detected fault signal scans are shown in Fig. 9.

The 3D analytical model provides a means to determine the detected QUAD signal by the Chattock for varying fault

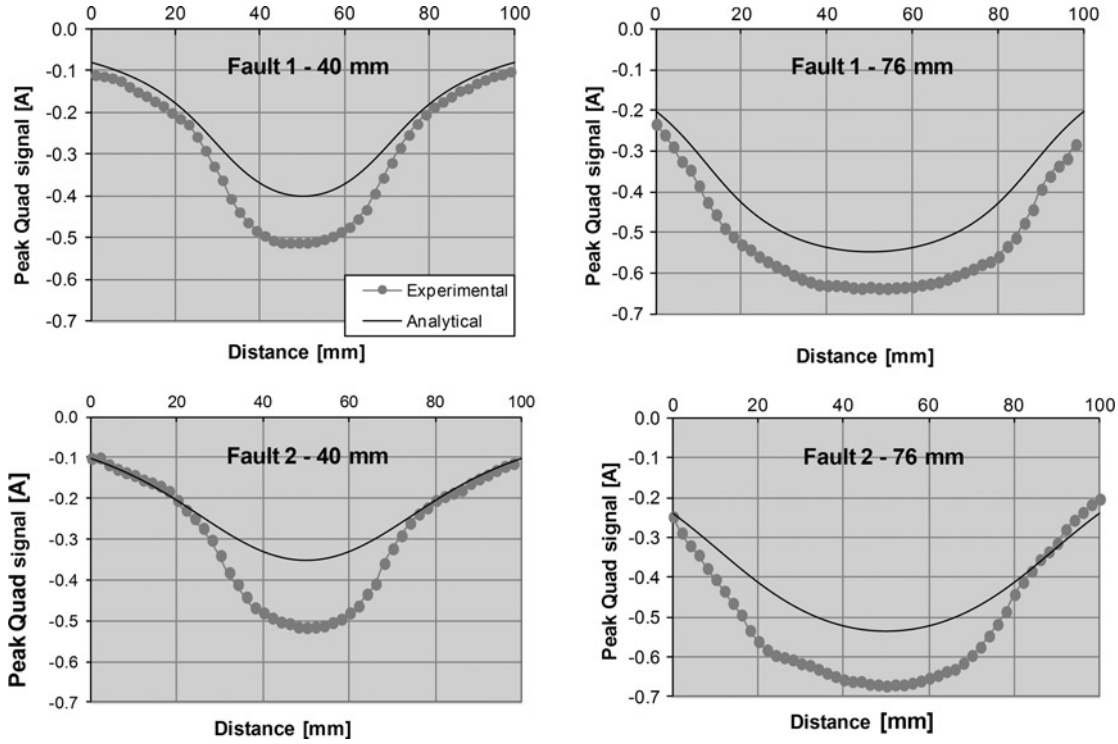

Fig. 10 *3D analytic and experimental plots for Faults 1 and 2 at 40 and 76 mm lengths*

doi: 10.1049/iet-epa.2011.0125

length, and as the Chattock is scanned across the fault. There is, as expected, substantial reduction in the detected signal compared to the actual current for short faults, however, larger than found in experimental practice. The reasons for this are discussed in Section 6.

6 Experimental test core and results

A short experimental stator core of the same geometry as the 2D model was constructed as a validation tool, with a main core packet of 76 mm in axial length with two outer 10 mm 'guard' packets. Good electrical contact down the back of the core was ensured at the keybars. Surface faults (faults 1 to 3) were imposed on the otherwise fault-free test core, using appropriate lengths of 0.45 mm diameter. NiCr wire clamped against cleaned, prepared, lamination edges. The excitation was adjusted to set the required 4% magnetic flux test level in the core. The 'fault current' was measured as the m.p.d. (Amps) detected conventionally by the Chattock coil and EL CID. It should be noted that this current will be less than the actual fault current since the Chattock coil only approaches 100% detection for infinite-length faults.

The QUAD fault current signals predicted by the 3D analytical model are illustrated in Fig. 10, and compared to those measured on the experimental test core for axial fault lengths of 40 and 76 mm for the two surface faults (1 and 2). In these results the Chattock coil spans the tooth that encloses the fault. As expected, the fault signal is greatest at the centre of the fault and then reduces as the sensor moves axially away from the fault centre.

The correlation between the experimental measurement and the 3D analytical model is thought to be very reasonable overall when one considers the electromagnetic complexity of the problem. The lower readings from the 3D analytic model can be attributed in the main to the use of a homogenous core compared to the normal laminated core in the experimental test. Sutton [10] has shown how the magnetic potentials from short faults are only slowly attenuated in the plane of the laminations, which would give this effect. Although the experimental model can not directly prove the fault current distribution, the general agreement of signal shape between model and experiment provides good evidence that the current is as uniform as shown earlier.

7 Conclusions

Non-invasive electromagnetic sensors can be used to determine stator core faults in large electrical machines, such as turbo-generators, hydro-generators and motors as part of a condition-based monitoring scheme. This paper develops a 2D analytic model of the current distribution in a stator core fault, demonstrating its substantial uniformity almost regardless of length. A 2D FE analysis validated the currents for infinite fault lengths, while also examining a series of different core fault locations. This demonstrated that almost all of these faults can be detected although as expected the signal levels reduce substantially as the faults become buried within the core back.

The paper further developed 3D analytical models able to determine the detection of finite-length surface faults, and how the detection efficiency varies with fault length. The results confirm that the Chattock sensor can identify short length core faults, and also demonstrates how the quadrature fault signal spatial response also changes depending upon the fault location, which can be used to assist an experienced operator in determining the likely position of the fault region.

The work was further verified using an experimental test core on which controlled lamination faults of varying axial length could be imposed. The experimental results correlated well with the fault signals predicted using the new 3D analytical model, subject to known simplifications necessary in the modelling. The results enhance the ability to differentiate between different types and location of faults through the physical insight provided by the fault models, and develops a deeper understanding of the electromagnetic behaviour of core faults.

8 Acknowledgments

The authors acknowledge the support for this work provided by Iris Power LP and by the Knowledge Transfer Partnership Scheme UK.

9 References

1 Stone, G.C., Boulter, E.A., Culbert, I., Dhirani, H.: 'Electrical insulation for rotating machines: design, evaluation, aging, testing and repair' (Wiley-Interscience, 2004)
2 Repair and Testing Guide for Generator Laminated Cores Grounded at the Core Outside Diameter, EPRI, Palo Alto, CA, 2002. 1007441
3 Murray, S.J., Edmonds, J.S., Foulds, J.R., Sire, R.A., Chi, W.-M.: 'Modeling fault propagation in an electric generator stator core' Eighth EPRI Steam Turbine Generator Workshop, EPRI, Nashville, TN, USA, 2003
4 Tallam, R.M., Lee, S.B., Stone, G.C., *et al.*: 'A survey of methods for detection of stator-related faults in induction machines', *IEEE Trans. Ind. Appl.*, 2007, **43**, (4), pp. 920–933
5 Romary, R., Jelassi, S., Brudny, J.F.: 'Stator-interlaminar-fault detection using an external-flux-density sensor', *IEEE Trans. Ind. Electron.*, 2010, **57**, (1), pp. 237–243
6 'IEEE Std 62.2.2004: 'Guide for diagnostic field testing of electric power apparatus', 2005
7 Sutton, J., Sasic, M., Bertenshaw, D.R.: '30 years experience with EL CID stator core testing'. Iris Rotating Machine Conf., Long Beach, CA, USA, 17 June 2008
8 Tallam, R.M., Lee, S.B., Stone, G.C., *et al.*: 'EL CID (Electromagnetic – core imperfection detector) testing of large steam-turbine-driven generators'. TR257, CIGRE, Paris, 2004
9 Chattock, A.P.: 'On a magnetic potentiometer', *Proc. Phys. Soc. London*, 1887, **9**, pp. 23–26
10 Sutton, J.: 'Theory of electromagnetic testing of laminated stator cores', *Insight – Br. J. Non-Destr. Test.*, 1994, **36**, (4), pp. 246–251
11 Bertenshaw, D.R. (Ed.): 'Analysis of stator core faults – a fresh look at the EL CID vector diagram. Hydro 2006; Porto Carras, Greece', *Int. J. Hydropower Dams*, 2006
12 Smith, A.C., Bertenshaw, D.R., Ho, C.W., Chan, T., Sasic, M.: 'Detection of stator core faults in large turbo-generators'. IEMDC2009, IEEE, Miami, FL, USA, 2009, pp. 911–918
13 Roger, J.-Y., Vrignaud, E., Henneron, T., Benabou, A., Ducreux, J.-P.: 'Electromagnetic modelling of short circuited coreplates', *COMPEL – Int. J. Comput. Math. Electr. Electron. Eng.*, 2009, **28**, (3), pp. 762–771
14 Henneron, T., Piriou, F., Roger, J.-Y.: 'An approach to determine the circulation of magnetic field in FEM computation code with vector potential formulation', *IEEE Trans. Magn.*, 2011, **47**, (5), pp. 1354–1357
15 Krebs, G., Henneron, T., Clenet, S., Bihan, Y.L.: 'Overlapping finite elements used to connect non-conforming meshes in 3-D with a vector potential formulation', *IEEE Trans. Magn.*, 2011, **47**, (5), pp. 1218–1221
16 Tavner, P.J., Anderson, A.F.: 'Core faults in large generators', *IEE Proc. Electr. Power Appl.*, 2005, **152**, (6), pp. 1427–1439